

Estimation of Key Sunquake Parameters through Hydrodynamic Modeling and Cross-correlation Analysis

JOHN T. STEFAN¹ AND ALEXANDER G. KOSOVICHEV^{1,2}

¹*Department of Physics, New Jersey Institute of Technology, University Heights, Newark, NJ 07102*

²*NASA Ames Research Center, Moffett Field, Mountain View, CA 94035*

ABSTRACT

Sunquakes are one of the more distinct secondary phenomena related to solar flares, where energy deposition in the lower layers of the Sun’s atmosphere excites acoustic waves easily visible in HMI dopplergrams. We explore two possible sources of sunquakes in the context of the electron beam hypothesis, as an instantaneous transfer of momentum and as a gradual applied force. We model the sunquake excitation and compare with five observed sunquake events using a cross-correlation analysis. We find that at least half the events studied are consistent with the electron beam hypothesis and estimate the energy required to excite the sunquakes to be within the range determined by previous studies.

Keywords: sunquakes — helioseismology — flares

1. INTRODUCTION

Solar flares represent some of the most energetic phenomena observed in the Solar System. It is well-understood that solar flares result from the reconfiguration of the local magnetic field towards a lower-energy state (Aschwanden 2019; Ulyanov et al. 2019), which drives particle acceleration and other secondary processes. A comprehensive understanding of energy transport in the solar atmosphere requires close inspection of these secondary processes, which distribute the energy released in flares at coronal heights to regions lower in the atmosphere. Among these processes are sunquakes, which are impulsive seismic events in the lower solar atmosphere. While the effects of sunquakes are easily seen in observations - first detected by expanding ripples in MDI dopplergrams (Kosovichev & Zharkova 1998; Kosovichev 2006) - the mechanism by which they are generated has yet to be determined.

Magnetic reconnection in the corona has been identified as the main driver of energy release during solar flares (Antiochos et al. 1999; Kopp & Pneuman 1976), and electron beams accelerated by this reconnection process are suggested as a possible means of exciting sunquakes (e.g. Sharykin et al. 2017; Macrae et al. 2018; Pedram & Matthews 2012). In particular, the thick-target model (e.g. Fisher et al. 1985) suggests that the electron beam strikes a stationary chromosphere, and the resulting thermalization of the electrons can be observed as a sharp increase in hard X-ray (HXR) emission. If the electron beam hypothesis is correct, then there should be some correlation between HXR emission as a function of time and the time of sunquake excitation.

Sunquakes themselves are studied as part of helioseismology, which is concerned with the propagation of acoustic waves of the Sun. The discipline separates the acoustic waves into three separate modes: pressure waves, also called p-modes; gravity waves, also called g-modes; and the f-mode, a surface propagating gravity wave which separates p- and g-modes in the dispersion relation. G-modes generally have frequencies less than 2 mHz, with p-modes having frequencies greater than 2 mHz. In power spectra of the Sun’s radial velocity field, the p-modes produce a distinct banded structure identified as the resonant modes between 2 and 5 mHz. Non-resonant acoustic waves above 5 mHz are usually referred to as pseudo-modes, as they appear as a similar banded structure in power spectra. Sunquakes generally produce higher frequency waves due to the short duration of excitation, and pseudo-modes are often observed following sunquakes because of this.

Previous studies of sunquakes have identified the photosphere or lower chromosphere as possible places of sunquake excitation (Zharkova & Zharkov 2015; Sharykin et al. 2017; Chen 2019). Furthermore, it appears that heating in these regions and the subsequent shocks can provide enough energy to excite the acoustic waves (Kosovichev 2015). Zharkova & Zharkov (2015) find that electron, proton, or mixed-particle beams have the potential to provide the necessary heating, that proton beams may penetrate up to 300 km below the quiet-sun photosphere, and that electron beams can penetrate as far as 5000 km below the photosphere.

In this work, we will examine the possibility of an electron beam as a sunquake source. We construct a hydrodynamic model and test two types of perturbations: an instantaneous transfer of momentum to the surrounding atmosphere - analogous to the shock excited by the thermalization of the electron beam - and a more gradual transfer of energy modeled as an applied external force. While the first type of source is more applicable for strong flares, where the emission is more impulsive, the second type of source may help to explain sunquakes generated by flares of lower class and more gradual high-energy emission. We place these sources in the low chromosphere and photosphere, where it is suspected that sunquakes are excited.

In addition to testing various sources, we also account for changes in the atmosphere through which resulting acoustic waves travel. In higher density regions, such as the chromosphere and photosphere, changes to acoustic wave propagation due to MHD effects are expected to be small as these contributions are relevant only when the Alfvén velocity is close to or greater than the acoustic sound speed. This occurs for low densities, but also for very large magnetic fields. The observed sunquakes we use to compare with our model propagate outside their respective active regions, so an MHD treatment of the acoustic waves is not necessary. We do, however, consider the effects of acoustic wave propagation through a damping medium by employing a damping scheme based on wavenumber, which we explore in more depth in section 2.4.

2. GOVERNING EQUATIONS AND METHODS

2.1. Governing Equations

To construct the model, we begin with the compressible mass continuity and momentum equations

$$\frac{D\rho}{Dt} + \rho \nabla \cdot \mathbf{v} = 0 \quad (1)$$

and

$$\frac{D}{Dt}(\rho \mathbf{v}) = -\nabla P + \rho \mathbf{g} + \mathbf{F}_{ext}, \quad (2)$$

where D/Dt is the material derivative and is equivalent to

$$\frac{D}{Dt} = \frac{\partial}{\partial t} + \mathbf{v} \cdot \nabla,$$

which includes changes in time and also gradients advected by the velocity field. We assume that processes which occur during acoustic wave propagation are slow and do not affect the entropy of the system, i.e. propagation is adiabatic such that

$$\frac{DS}{Dt} = \frac{D}{Dt} \left(\frac{P}{\rho^\gamma} \right) = 0. \quad (3)$$

We will consider linear Eulerian perturbations to the above equations, such that the background state is assumed to be time-independent and contains only radial variations: $\rho \rightarrow \rho_0(r) + \rho'(r, \vartheta, \varphi, t)$. We choose the case where there are no background velocity fields, and so the fluid velocity is itself a perturbation: $\mathbf{v} \rightarrow \mathbf{v}(r, \vartheta, \varphi, t)$. Furthermore, we separate the velocity into radial and horizontal components, where the horizontal component contains both the $\hat{\theta}$ and $\hat{\phi}$ components. Finally, we assume that the radial and ϑ, φ dependence can be separated as

$$a(r, \vartheta, \varphi) = a(r)Y_l^m(\vartheta, \varphi),$$

where the Y_l^m are the spherical harmonics.

Beginning with the equation for mass conservation, equation 1, we expand the variables in terms of their background and perturbed quantities. Keeping only linear terms, expanding derivatives, and separating the radial and horizontal divergence ($\nabla_{\mathbf{h}}$), we arrive at

$$\frac{\partial \rho'}{\partial t} + v_r \frac{\partial \rho_0}{\partial r} + \rho_0 \left(\frac{1}{r^2} \frac{\partial}{\partial r} (r^2 v_r) + \frac{1}{r} \nabla_{\mathbf{h}} v_{\mathbf{h}} \right) = 0.$$

We choose the case where the angular dependence of v_h can be separated as $v_h(r, t) \Delta_{\mathbf{h}} Y_l^m(\vartheta, \varphi)$, where $\Delta_{\mathbf{h}}$ is the horizontal gradient, and express the equation with any associated dependences

$$\left[\frac{\partial \rho'(r, t)}{\partial t} + v_r(r, t) \frac{\partial \rho_0(r)}{\partial r} + \rho_0(r) \frac{1}{r^2} \frac{\partial}{\partial r} (r^2 v_r(r, t)) \right] \cdot f(\vartheta, \varphi) + \rho_0(r) \left[\frac{v_h(r, t)}{r} \right] \nabla_h^2 Y_l^m(\vartheta, \varphi) = 0.$$

It is convenient to choose the case where the sunquake is centered over the pole at $\vartheta = 0$, as the system is then azimuthally symmetric and the spherical harmonics reduce to the associated Legendre polynomials $P_l(\cos \vartheta)$. In this case, the term $\nabla_h^2 P_l$ is equivalent to $-L^2 P_l = -l(l+1)P_l$ and no angular derivatives need to be explicitly computed. We will use the shorthand $x_l = A_l x$, where the variable x_l is any variable x with its associated Legendre coefficients A_l . Making the appropriate substitutions and dividing through by ρ_0 we arrive at

$$\frac{\partial \bar{\rho}_l}{\partial t} + v_{r,l} \frac{\partial \ln(\rho_0)}{\partial r} + \frac{1}{r^2} \frac{\partial}{\partial r} (r^2 v_{r,l}) - \frac{L^2}{r} v_{h,l} = 0, \quad (4)$$

where $\bar{\rho} = \rho'/\rho_0$ is the normalized perturbation to density.

We move now to the energy equation, 3; expanding the material derivative, expressing the variables in terms of background and perturbed quantities, removing non-linear terms, and keeping in mind that background pressure and density vary only in the radial direction, we have

$$\frac{1}{\gamma P_0} \frac{\partial P'}{\partial t} + v_r \left(\frac{1}{\gamma P_0} \frac{\partial P_0}{\partial r} - \frac{1}{\rho_0} \frac{\partial \rho_0}{\partial r} \right) = \frac{1}{\rho_0} \frac{\partial \rho'}{\partial t}.$$

Note that the Brunt-Väisälä frequency (N), or buoyancy frequency, is defined as

$$N^2 = g \left(\frac{1}{\gamma P_0} \frac{\partial P_0}{\partial r} - \frac{1}{\rho_0} \frac{\partial \rho_0}{\partial r} \right).$$

The buoyancy frequency determines the frequency and stability of gravity waves; in the solar core, this frequency is real-valued and produces internal g-modes. In the convective region, this frequency is imaginary, and corresponds to exponentially decaying or growing waves. We make the buoyancy frequency substitution in the energy equation

$$\frac{1}{\gamma} \frac{\partial \bar{P}}{\partial t} + v_r \frac{N^2}{g} = \frac{\partial \bar{\rho}}{\partial t},$$

where $\bar{P} = P'/P_0$ is the normalized perturbation to pressure. Replacing the normalized density time-derivative with equation 4, and substituting the Legendre polynomials, we find the final form for the energy equation

$$\frac{\partial \bar{P}_l}{\partial t} + \gamma \left[v_{r,l} \left(\frac{N^2}{g} + \frac{\partial \ln(\rho_0)}{\partial r} \right) + \frac{1}{r^2} \frac{\partial}{\partial r} (r^2 v_{r,l}) - \frac{L^2}{r} v_{h,l} \right] = 0. \quad (5)$$

Lastly, we begin our treatment of the momentum equation by first separating the radial and horizontal components, and performing the same expansion as for equations 4 and 5. Looking first at the radial momentum equation

$$\rho_0 \frac{\partial v_r}{\partial t} = -\frac{\partial P_0}{\partial r} - \frac{\partial P'}{\partial r} + \rho_0 g + \rho' g + F_{ext,r}.$$

We assume that the background state is in hydrostatic equilibrium, which satisfies the relation $\partial P_0/\partial r + \rho_0 g = 0$, and these terms then fall out of the equation. Dividing through by ρ_0 to isolate the time-derivative and substituting the Legendre polynomials leaves us with

$$\frac{\partial v_{r,l}}{\partial t} = -\frac{1}{\rho_0} \frac{\partial P'_l}{\partial r} + \bar{\rho}_l g + \frac{F_{ext,r,l}}{\rho_0}. \quad (6)$$

The horizontal component of the momentum equation has the original form

$$\rho_0 \frac{\partial v_h}{\partial t} = \frac{1}{r} \Delta_h P' + F_{ext,h}.$$

When expanding the variables in terms of radial and angular dependence, we note that P' varies only in time and in radius, so the horizontal gradient is moved to the right and applied to the Legendre polynomials. We assume that external horizontal forces can be decomposed as $F_{ext,h} = F_{ext,h}(r, t) \Delta_h P_l(\vartheta, \varphi)$, and so $\Delta_h P_l$ can be entirely removed from the equation. Dividing through by ρ_0 yields the final form

$$\frac{\partial v_{h,l}}{\partial t} = \frac{P'_l}{r \rho_0} + \frac{F_{ext,h,l}}{\rho_0}. \quad (7)$$

2.2. Boundary Conditions

Acoustic waves which propagate at or above the acoustic cut-off frequency, ω_c , travel through the solar surface and are mostly damped in the atmosphere (Christensen-Dalsgaard 2002). Waves which propagate below this frequency are reflected at the surface and are resonant. To implement this selective resonant behavior in the model, we must choose our boundary conditions carefully. Using Dirichlet boundary conditions leads to reflections at the upper computational domain, and it is not entirely clear how Neumann boundary conditions can be formulated a priori to minimize reflections.

We therefore derive non-reflecting boundary conditions by performing an eigendecomposition of the matrix B which contains the radial derivatives of our system. To simplify calculations, we include only equations 5 and 6; this is reasonably justified since ρ' and P' are essentially equivalent through equation 3, and equation 7 contains no radial derivatives. The matrix form of the simplified system is given by

$$A \frac{\partial \mathbf{X}}{\partial t} + B \frac{\partial \mathbf{X}}{\partial r} = \mathbf{C},$$

where A is the matrix containing time-derivative coefficients, $\mathbf{X} = [P'_l, v_{r,l}]^T$ are the variables, and \mathbf{C} is the vector containing constants. We choose to use the form of equation 5 where pressure perturbations are not normalized, and the matrix A is then simply the identity matrix. The radial-derivative matrix B then has the form

$$B = \begin{bmatrix} 0 & \gamma P_0 \\ \frac{1}{\rho_0} & 0 \end{bmatrix},$$

Which has eigenvalues $\lambda_+ = +c_s$ and $\lambda_- = -c_s$, where $c_s = \sqrt{\gamma P_0 / \rho_0}$ is the adiabatic sound speed. With these eigenvalues we obtain the eigenvalue decomposition

$$B = \frac{1}{2} \begin{bmatrix} \rho_0 c_s & -1 \\ 1 & \frac{c_s}{\gamma P_0} \end{bmatrix} \begin{bmatrix} +c_s & 0 \\ 0 & -c_s \end{bmatrix} \begin{bmatrix} \frac{c_s}{\gamma P_0} & 1 \\ -1 & \rho_0 c_s \end{bmatrix}.$$

Performing the matrix multiplication within B and keeping terms separate allows us to determine which derivatives correspond to the inward propagating waves. For these terms, we enforce hydrostatic equilibrium for the perturbed quantities ($[\partial P'_l / \partial r] = -\rho' g$ and $[\partial v_{r,l} / \partial r] = 0$) so that these derivatives need not be evaluated. The boundary conditions for $R = R_{max}$ used are then

$$\begin{cases} \frac{\partial \bar{\rho}_l}{\partial t} + v_{r,l} \left(\frac{\partial \ln \rho_0}{\partial r} + \frac{2}{r} \right) - \frac{L^2}{r} v_{h,l} + \frac{1}{2} \left(c_s \frac{\partial \bar{\rho}_l}{\partial r} + \frac{\partial v_{r,l}}{\partial r} + \frac{\bar{\rho}_l g}{c_s} \right) = 0 \\ \frac{\partial \bar{P}'_l}{\partial t} + \gamma \left(v_{r,l} \frac{\partial \ln \rho_0}{\partial r} + v_{r,l} \frac{N^2}{g} - \frac{L^2}{r} v_{h,l} \right) + \frac{1}{2} \left(c_s \frac{\partial \bar{\rho}_l}{\partial r} + \frac{\partial v_{r,l}}{\partial r} + \frac{\bar{\rho}_l g}{c_s} \right) = 0 \\ \frac{\partial v_{r,l}}{\partial t} + \bar{\rho}_l g + \frac{1}{2} \left(c_s^2 \frac{\partial \bar{\rho}_l}{\partial r} + c_s \frac{\partial v_{r,l}}{\partial r} - \bar{\rho}_l g \right) = 0 \\ \frac{\partial v_{h,l}}{\partial t} + \frac{P'_l}{r \rho_0} = 0 \end{cases},$$

where we have made the substitution $P'_l = c_s^2 \rho'_l$.

2.3. Numerical Methods

The governing equations are solved along a radial mesh containing values for radius, background density, background pressure, adiabatic exponent, and gravitational acceleration. The mesh used for the simulations is the Standard Solar Model as described by Christensen-Dalsgaard et al. (1996), which is computed to $R = 696.841$ Mm.

The time derivatives are approximated by a first order forward difference

$$\frac{\partial y}{\partial t} \approx \frac{y_i^{n+1} - y_i^n}{\tau},$$

where τ is the time step chosen to satisfy the CFL condition (Courant et al. 1967) $\tau_{CFL} \leq \min[\Delta x / c_s]$, corresponding to the travel time of an acoustic wave between the shortest grid point separation Δx . We choose to use $\tau = 0.6 \tau_{CFL}$

for stability. The radial derivatives are approximated by a fourth order central difference, which has the following form for a uniform grid

$$\frac{\partial y}{\partial r} \approx \frac{y_{i-2}^n - 8y_{i-1}^n + 8y_{i+1}^n - y_{i+2}^n}{12\Delta x}.$$

We use a non-uniform grid, however, and the appropriate coefficients and grid separations are substituted. We employ a staggered mesh scheme, where the pressure, density, and horizontal velocity variables are placed on "body" points, and the radial velocity variable is placed on "edge" points halfway between two body points; i.e. $r_{b,i} < r_{e,i} < r_{b,i+1}$. Values for pressure and density are computed first, followed by the radial and horizontal velocities using the updated pressure and density values.

2.4. Damping by Wavenumber

Our governing equations have so far neglected any effects from viscous damping, as the plasma viscosity is highly dependent on ionization, temperature, and magnetic field strength (Vranjes 2014), which are outside the scope of this research. We instead choose to use an ad hoc damping scheme, where acoustic waves are damped by wavenumber, and appropriate parameters are derived from observation. We assume that acoustic waves traveling with frequency ω_0 have time-dependence of the form $\Psi(t) = A \exp[i\omega_0 t] \exp[-\alpha_l t]$, where α_l is a damping parameter dependent on the angular degree l associated with the frequency ω_0 . The angular degree and horizontal wavenumber are closely related by $k_h = \sqrt{l(l+1)}/R_\odot$, and we choose to evaluate α_l in terms of the angular degree since our governing equations are solved in this way as well.

The power spectrum of the signal is dependent on frequency as

$$P = \frac{A}{4\pi^2} \frac{1}{(\omega_0 - \omega)^2 + \alpha_l^2}.$$

Note that the power is maximized at the frequency ω_0 . Evaluating the power at the upper frequency (ω_+) of the full-width, half-maximum ($FWHM = 2(\omega_0 - \omega_+)$) and equating with P_{max} shows the damping parameter is $\alpha_l = (1/2)(FWHM)$. The associated damping time (τ_l) is the inverse of α_l . For simplicity, we assume that the damping time varies with l as

$$\tau_l = \tau^* \left(\frac{l}{l^*} \right)^\gamma,$$

where l^* is an arbitrary base angular degree, τ^* is the damping time of the base angular degree, and γ is a power-law exponent derived from observations.

We consider three damping cases: quiet-sun damping, active-region damping, and no damping. For the first case, we use p-mode data from E J Rhodes et al. (2011), in which a three day full-disk dopplergram series is used to compute an azimuthally averaged power spectrum. The damping times are derived from the FWHM data of the set, and the obtained damping times are fit to a power law using a least-squares algorithm to derive the index. We find $\gamma = -0.723$ and for the chosen base $l = 1000$, the damping time is 843 seconds. For active-region damping, we assume that only the damping times change, and the exponent γ remains constant. The power spectrum of a three-hour dopplergram series of AR 11598 (figure 1a) is used to obtain the damping time for the base angular order $l = 800$, which is chosen instead of $l = 1000$ as this degree is not well-resolved from the background. There are two discernable peaks in the $l = 800$ power spectrum (figure 1b), and fitting with a Gaussian profile yields a damping time of 408 seconds for the first peak and 422 seconds for the second; we use the average of 415 seconds as the base τ^* .

2.5. Source Functions

We consider two types of perturbations to the governing equations, momentum perturbations and applied external forces. The momentum perturbations are instantaneous, and the external force perturbations are time-dependent, which we use to simulate gradual processes. All perturbations are directed in the downward radial direction, and have Gaussian radial and angular dependences; the time dependence of the force perturbations are also Gaussian. In the general case, force perturbations have the form

$$F_r(r, \vartheta, t) = A \exp \left[-\frac{(r - r_0)^2}{2\sigma_r^2} \right] \exp \left[-\frac{\vartheta^2}{2\sigma_\vartheta^2} \right] \cdot \exp \left[-\frac{(t - t_0)^2}{2\sigma_t^2} \right] \hat{\mathbf{r}},$$

where σ_r , σ_ϑ , and σ_t are parameters related to the full-width half-maximum of the respective Gaussians, r_0 is the radial center of the source, $t_0 = T/2$ is the central time chosen to be half the duration of the source, the duration $T = 200$ s,

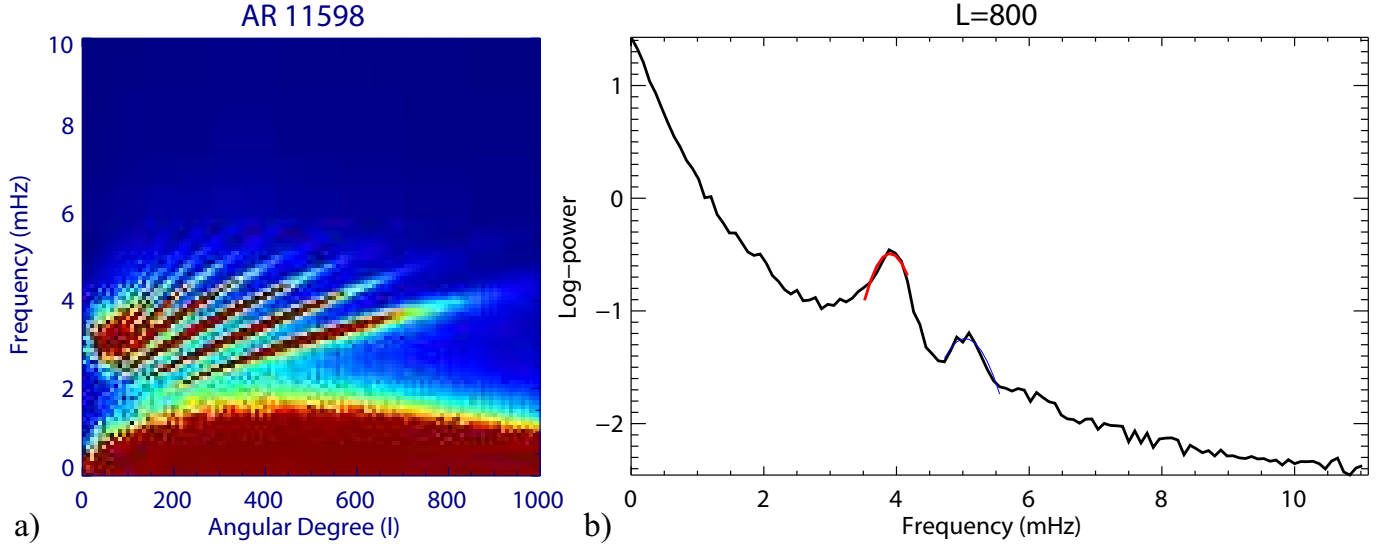


Figure 1. (a) Power spectrum obtained from the Dopplergram series of AR 11598. (b) Power spectrum of angular degree $l = 800$. The first peak (in red) corresponds to $\tau_{800} = 408$ seconds, and the second peak (in blue) corresponds to $\tau_{800} = 422$ seconds.

$\sigma_r = 0.2$ Mm, and the amplitude A is arbitrary and negative, chosen to be -0.001 dyn cm $^{-3}$. Momentum perturbations are identical, and have the time dependence removed; again, the amplitude is arbitrary and negative, though a value of $-100\rho_0(r)$ g m s $^{-1}$ is chosen, where $\rho_0(r)$ is the background density at a given grid point. Additionally, the σ_θ parameter is fixed at 8.6×10^{-4} radians, which corresponds to a circular area on the surface ($R = 695.9906$ Mm) with radius 0.6 Mm.

3. RESULTS

3.1. Differences Between Force and Momentum Sources

We first examine the relationship between force and momentum perturbations, as we expect there to be a 90 degree phase difference between the time-distance diagrams of the two sources. We observe this phase difference, which can be seen clearly in figure 2, and note that it persists regardless of source depth. Interestingly, the phase difference is actually -90 degrees, as differentiation with respect to time of the momentum source signal yields a 180 degree phase difference (figure 2). Furthermore, we find that the ray path predicted by asymptotic theory (which defines the beginning of the wavepacket) marks separate phases in the two sources' propagation because of the phase difference. For force perturbations, the ray path travels with the beginning of the sunquake wavepacket; for momentum sources, however, the ray path travels with the location of greatest acceleration in the first peak. The signals of the two sources are separated by several minutes, well within HMI resolution, and if the start time of the sunquake is known, then matching the ray path with the sunquake's time-distance diagram may be useful in determining what type of source initiated the quake.

Additionally, we find that the appearance of the time-distance diagrams of the two sources are completely distinct (figure 3). For comparison, we center force and momentum perturbations at $R = 696.119$ Mm with $\sigma_r = 0.2$ Mm. The first bounce signal of the undamped time-dependent force perturbation appears to be longer than that of the momentum perturbation, and also has more complicated structure. Both models produce g-modes, which propagate in a similar fashion to shallow water gravity waves. In linear acoustics the solar atmosphere is stable to gravity wave propagation (figure 4), though these waves - especially of such strength - have not been observed. This may be due to non-linear effects, or break-up caused by convective upflows and downflows. The g-modes in the force perturbation model are stronger and more coherent than in the momentum perturbation model. The model also reproduces the ordinary surface propagating wave (f-mode), which is regularly observed (Singh et al. 2016), and in the model precedes the shallow water waves. The f-mode is more prominent in momentum perturbations and there is longer time delay between f-mode and g-mode arrival as compared to the force perturbations.

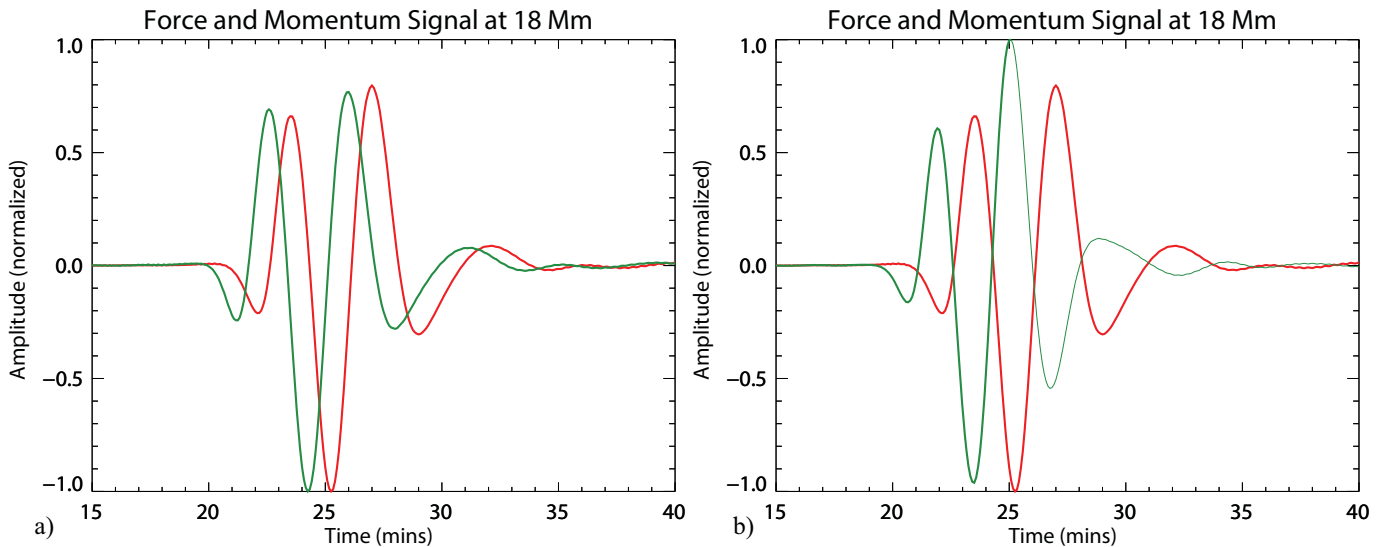


Figure 2. (a) Normalized radial velocity measured at a distance of 18 Mm from the source, for momentum (green) and force (red) sources. (b) Normalized radial velocity time-derivative (green) of the momentum perturbation and radial velocity of the force perturbation (red).

As damping is increased, the g-modes are affected more heavily than the seismic wave, though the consecutive bounces of the seismic wave and the f-mode show decreases in amplitude. The general phase relationship between momentum perturbation seismic signals is preserved, though it appears to be smoothed, with shorter wavelength features blending into the longer wavelength features. The force perturbation model shows similar smoothing and the first bounce signal is stretched into two main packets. This separation into two packets increases in the active region damped case, and the g-mode in this case is almost entirely damped. The g-mode damping is also present in the active region damped momentum perturbation, though the g-modes are damped stronger in this case. In both models the f-mode is also entirely damped, and consecutive bounces are barely measurable. We note that there is some corruption of signal near the origin, which is caused by the damping on higher wavenumbers, leading to the loss of small-scale resolution and a blurring effect.

3.2. Observational Comparisons

We also compare our results with a number of observed sunquakes, which are the events associated with the X1.8 flare in October 2012, the X9.3 flare in September 2017, the X3.3 flare in November 2013, the X1.0 flare in March 2014, and the M1.1 flare in September 2015 (Table 1) from the sunquake catalog of Sharykin & Kosovichev (2019).

Table 1. Sunquake Events and Relevant Times

GOES Flare Class	Date	T_{start} (UT)	Lon. [†] (deg)	Lat. [†] (deg)	T_{G1} (s)	T_{G3} (s)	T_{BP} (s)
X1.8	2012 Oct 23	03:16:30	110.3	-12.7	+85	+141	+45
X9.3	2017 Sep 6	11:57:00	122.6	-9.1	-82	-49	-60
X3.3	2013 Nov 5	22:10:19	175.5	-12.6	+34	+76	+56
X1.0	2014 Mar 29	17:45:00	132.5	+32.0	+17	+48	+135
M1.1	2015 Sep 30	13:15:00	108.0	-21.0	+86	+48	N/A

Sunquake events used for comparison, where the start time is the beginning time of the Dopplergram series. The flare relevant times are listed as a time shift relative to the start time of the Dopplergram series. [†] Latitude and longitude are given in heliographic coordinates.

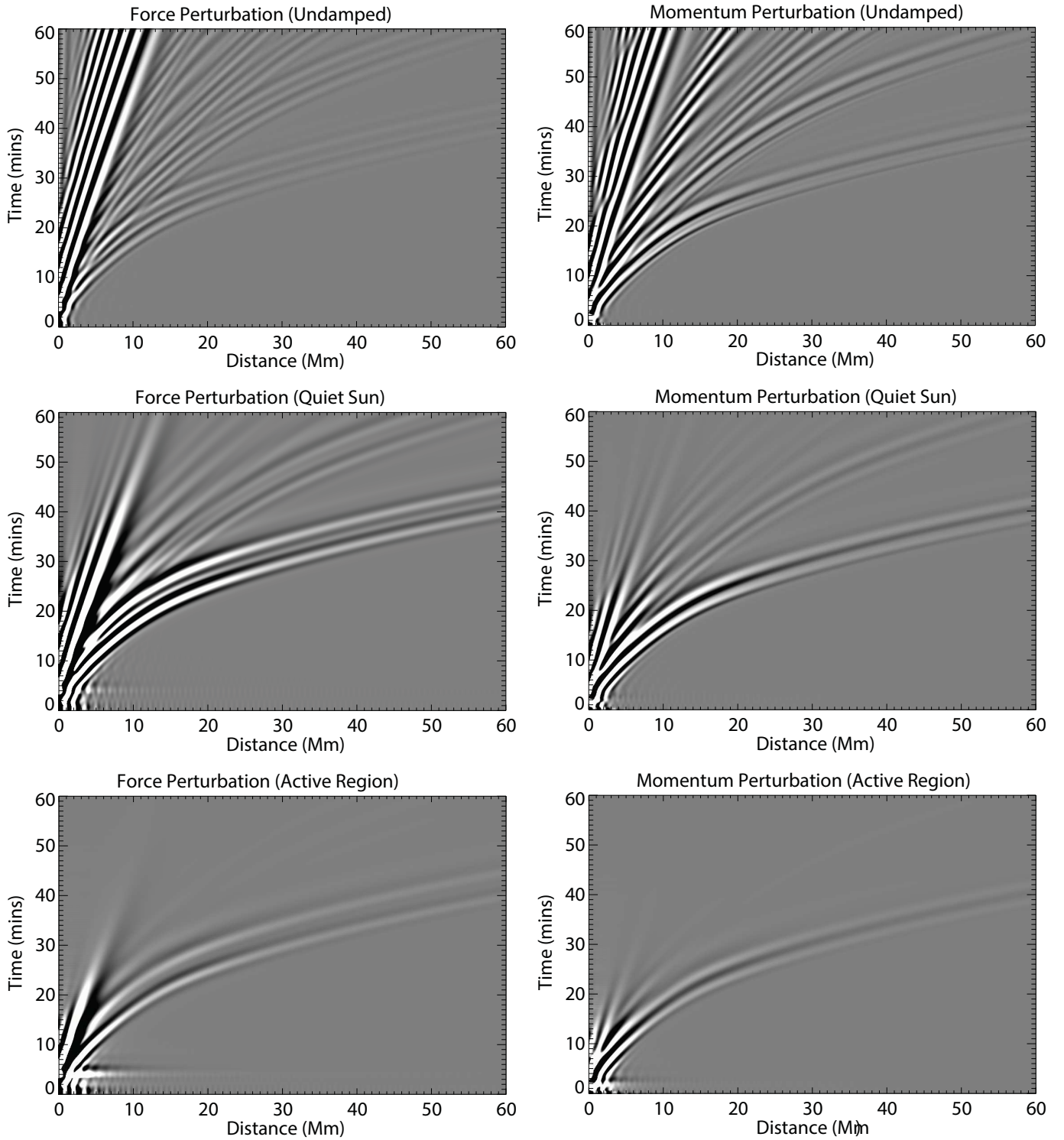


Figure 3. (Left column) Force perturbations with increasing damping: undamped, quiet-sun damped, and active region damped, respectively. (Right column) Momentum perturbations with increasing damping: undamped, quiet-sun damped, and active region damped, respectively.

Time-distance diagrams are produced for these events using data from the Helioseismic and Magnetic Imager (HMI) from Solar Dynamics Observatory (SDO) (Scherrer et al. 2012), after a frequency filter with a Gaussian cut-off is applied to the dopplergram series. The central frequency and width of the filter vary, and are chosen to increase the

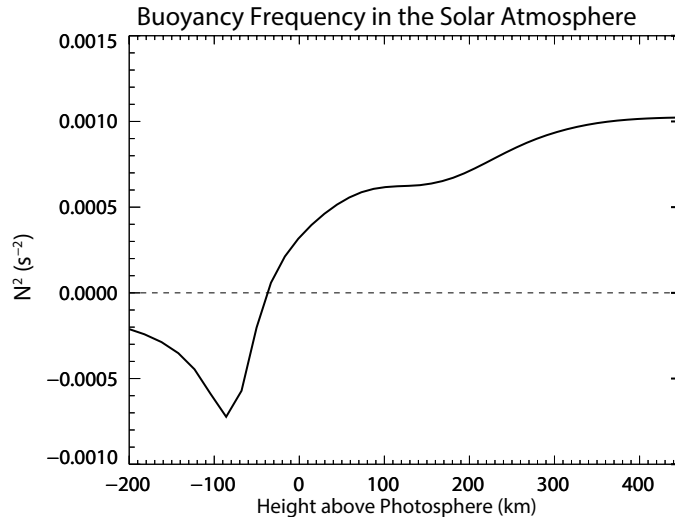


Figure 4. Square of the buoyancy frequency as a function of height in the solar atmosphere, with $z=0$ km being the base of the photosphere. Negative values correspond to unstable g-mode propagation and positive values indicate stable regions of g-mode propagation.

contrast of the sunquake signal from the background convective noise. Time-distance diagrams are also produced from the model runs, and are treated with an identical filter for comparison. The model runs used in the comparison are separated into two sets, one of momentum perturbations and one of force perturbations. Each set contains 46 modeled sunquakes with fixed radial width centered along the grid points of the Standard Solar Model, corresponding to the range of $R=695.788$ Mm to $R=696.422$ Mm.

In increments of 1 Mm along the horizontal axis, the cross-correlation of the observed sunquake to the set of modeled sunquakes is computed as a function of time-shift (τ) and distance-shift (ξ). The cross-correlation is then dependent on four parameters: time-shift, distance-shift, source depth (z), and distance from source (d). The cross-correlation is averaged over distance from the source, and the set of cross-correlations which are maximized with respect to distance-shift are identified. The resulting cross-correlation function is dependent only on time-shift and source depth, and a best fit is identified based on which parameters maximize the cross-correlation. The ratio of the model and observed maximum velocities within the first-bounce wave packet is used to obtain an estimate for the source amplitude, which in turn is used to estimate transferred kinetic energy.

We examine the results of the computation in the context of three main times: 1) When the time-derivative of SXR emission is at its maximum; 2) The time when the HXR emission is at its maximum; and 3) the start time of the sunquake as determined from HMI so-called "bad pixels". In HMI dopplergrams, there appear pixels which have wildly different values from their neighbors, and are often called bad pixels or anomalous pixels. These pixels appear as a failure of algorithms to correctly interpret filtergram data during Level 1 processing, and are associated with extreme values of doppler velocity, magnetic field, and other observables (Couvidat et al. 2016). We interpret these pixels as the source location of sunquakes, and their first appearance as the start time (T_{BP}) of the sunquake.

The HXR and $dSXR/dt$ peak times are obtained from KONUS-WIND data (Aptekar et al. 1995; Lysenko et al. 2018), which observes in three bands: G1 in the 21-82 keV range, G2 in the 82-331 keV range, and G3 in the 331-1252 keV range. The time derivative of the G1 band is used to find the $dSXR/dt$ peak (T_{G1}) and the peak of the G3 curve is associated with the HXR peak (T_{G3}). These times, and the timing of bad pixel appearance, are listed in Table 1; we note that bad pixels could not be identified in the M1.1 sunquake.

The best fit parameters from the cross-correlation analysis using the momentum and force sources are listed in Tables 2 and 3, respectively; the two-dimensional cross-correlations for the quiet-sun damped momentum and force perturbations are displayed in Figures 5 and 6, respectively. As a result of the periodicity in the signal, more than one band of best fit is often present. For momentum sources, a majority of undamped sunquakes have energies bounded by 1×10^{28} ergs and source amplitudes on the order of 10 km s^{-1} . There does not seem to be an easily identifiable height at which these types of sources may excite sunquakes, though the source height consistently decreases when damping is increased.

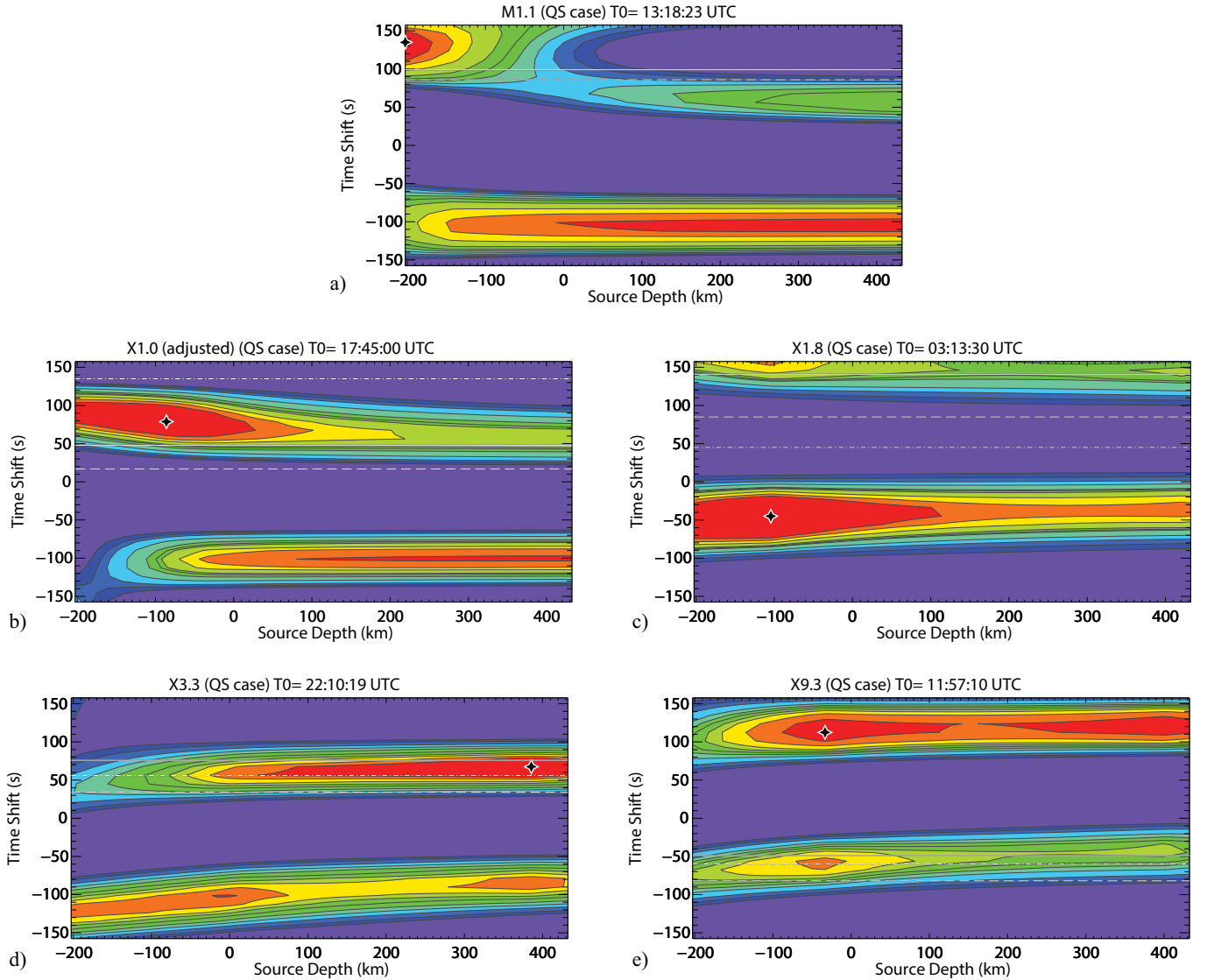


Figure 5. Cross-correlation functions with the quiet sun damped momentum perturbation model set. (a) Sunquake associated with the M1.1 flare; (b) Sunquake associated with the X1.0 flare; (c) Sunquake associated with the X1.8 flare; (d) Sunquake associated with the X3.3 flare; (e) Sunquake associated with the X9.3 flare. The contours begin at the median value, and each successive contour represents an increase in 5 percentile points (i.e. 50th, 55th, 60th, etc. percentiles). The solid horizontal line shows the HXR peak time, the dashed horizontal line shows the dSXR/dt peak time, and the dot-dashed horizontal line shows the suspected sunquake start time based on bad pixel count. The white and black diamond indicates where the parameters produce the greatest cross-correlation, and is used for energy estimation.

When the observed sunquake events are compared with the force perturbation set, the same relationship between source height and damping intensity remains. The amount of energy required to excite sunquakes in this way is also on the order 1×10^{28} ergs, and the energy estimates are more regular as damping is increased. Additionally, the bands of best fit for the force perturbation set are offset relative to those of the momentum perturbation set. This is consistent with the previous finding that force and momentum perturbations produce sunquakes offset by two to three minutes, and is related to the -90 degree phase difference between the two signals.

The cross-correlation method does produce bands in close proximity to time shifts related to important moments in flare evolution, such as the HXR peak time. In two of the five sunquake events compared with the undamped momentum set, the best-fit source begins immediately following the HXR peak (the M1.1 and X1.0 event). This count increases to three in the quiet-sun case (including the X3.3 event), and reduces to 2 for active region damping. For

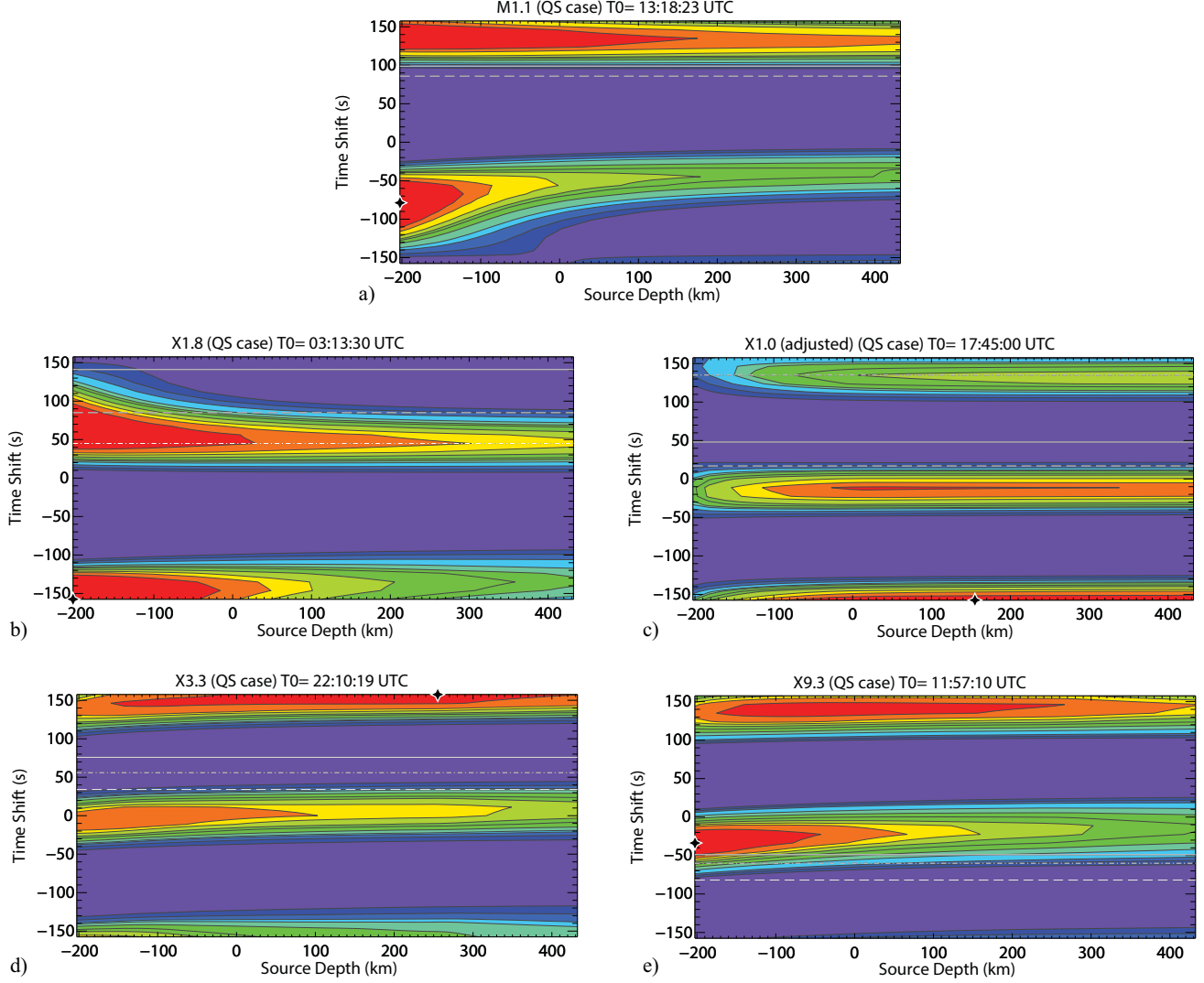


Figure 6. The same as in Fig. 5 for the force perturbation.

force perturbations, the undamped case has two best-fit sources close to the HXR peak, and one in the quiet sun and active region damping cases.

4. DISCUSSION AND CONCLUSIONS

It is expected that the sunquake source location moves downwards as damping is increased, since excitement of acoustic waves in these lower layers will increase their amplitude once the waves reach the lower densities of higher atmospheric layers. This plays a role in the large amounts of energy required to excite the sunquakes in heavily-damped regions, as well as the increase in source amplitude needed to produce acoustic waves with the observed amplitudes. In particular, the active region damping is not necessarily representative of conditions for some sunquakes, as three of the five sunquakes were excited along the polarity inversion line, where the radial magnetic field is small. The remaining sunquake events were excited at the edge of the respective active regions and propagated towards regions of lower magnetic field. The active region damping is particularly applicable in sunquake events where the acoustic waves travel across sunspot or active regions, though these types of events are difficult to observe and were not included in this study.

Additionally, the energy estimates are reliable only when the identified source coincides with or follows the HXR peak or bad pixel times, when the electron beam hypothesis is valid; we do not expect sunquake events to precede the HXR peak, which is a clear indication of energy deposition. The cases where this criteria is met include the M1.1,

Table 2. Best Fit Parameters for Sunquake Events - Momentum Source

		Momentum Case				
Flare	Damping	T_{shift} (s)	Height (km)	Amp. (g cm s^{-1})	Max. V (km s^{-1})	Energy (ergs)
X1.8	Undamped	-45	-17	1.95×10^{22}	11.1	6.39×10^{27}
	Quiet Sun	-45	-104	3.31×10^{23}	141.8	1.39×10^{30}
	Active Region	-56.25	-142	1.76×10^{24}	675.6	3.53×10^{31}
X9.3	Undamped	+112.5	+432	5.40×10^{21}	32.5	3.05×10^{27}
	Quiet Sun	+112.5	-33	1.54×10^{23}	82.3	3.74×10^{29}
	Active Region	+112.5	-68	1.54×10^{24}	785.8	3.82×10^{31}
X3.3	Undamped	+135	+386	2.68×10^{21}	11.5	5.88×10^{26}
	Quiet Sun	+67.5	+386	2.83×10^{22}	121.2	6.57×10^{28}
	Active Region	-123.75	-162	1.65×10^{24}	599.8	2.94×10^{31}
X1.0	Undamped	+67.5	+87	2.87×10^{22}	24.0	1.94×10^{28}
	Quiet Sun	+78.75	-86	9.48×10^{23}	430.2	1.21×10^{31}
	Active Region	+78.75	-123	6.96×10^{24}	2825.6	5.85×10^{32}
M1.1	Undamped	+101.25	-182	4.60×10^{22}	15.8	2.15×10^{28}
	Quiet Sun	+135	-203	7.34×10^{23}	238.8	5.19×10^{30}
	Active Region	+123.75	-203	5.47×10^{24}	1780.1	2.88×10^{32}

Table 3. Best Fit Parameters for Sunquake Events - Force Source

		Force Case			
Flare	Damping	T_{shift} (s)	Height (km)	Amp. (dyn cm^{-3})	Energy (ergs)
X1.8	Undamped	-146.25	-203	1.38×10^{-2}	1.01×10^{28}
	Quiet Sun	-157.5	-203	1.01×10^{-1}	5.58×10^{28}
	Active Region	-157.5	-203	6.59×10^{-1}	2.58×10^{29}
X9.3	Undamped	+135	+129	2.19×10^{-3}	2.27×10^{27}
	Quiet Sun	-33.75	-203	2.29×10^{-1}	1.27×10^{29}
	Active Region	-45	-203	1.57	6.17×10^{29}
X3.3	Undamped	+135	+181	5.65×10^{-4}	6.44×10^{26}
	Quiet Sun	+157.5	+255	1.30×10^{-2}	1.32×10^{28}
	Active Region	0	-33	4.24×10^{-1}	2.07×10^{29}
X1.0	Undamped	-157.5	+327	3.59×10^{-3}	4.56×10^{27}
	Quiet Sun	-157.5	+155	5.34×10^{-2}	4.73×10^{28}
	Active Region	-11.25	+432	6.52×10^{-1}	3.73×10^{29}
M1.1	Undamped	+146.25	-203	4.04×10^{-2}	2.93×10^{28}
	Quiet Sun	-78.5	-203	2.59×10^{-1}	1.44×10^{29}
	Active Region	-90	-203	1.45	5.68×10^{29}

X1.0, and X3.3 events in the case of an instantaneous momentum source, and the M1.1 and X9.3 events in the case of an external force source. In both source cases, the X1.8 has a band of best fit in conjunction with the HXR, dSXR/dt, and bad pixel times, but no points in the band maximize the cross-correlation.

In the successfully analyzed events of momentum sources, the energy required to excite the quake without damping is on order of 1×10^{28} ergs, consistent with recent estimates of [Chen \(2019\)](#) using acoustic holography methods. Furthermore, the energy estimate of a force source for the M1.1 event is nearly equivalent to the momentum source

counterpart. In the case of the X3.3 event, the undamped momentum source timing is not coincident with the HXR or bad pixel times, though increasing the damping temporally aligns the source nearly exactly with the HXR peak time. This quiet sun damping case also gives an energy estimate on the order of 1×10^{28} ergs, up to a maximum of 1×10^{29} ergs for the active region damped case which also provides a source coincident with the HXR peak time. Similar circumstances arise for the X9.3 case with an external force source, where the undamped source is unrelated temporally with any main times but the quiet sun damping indicates a source time just following the HXR peak time. The energy estimate for the X9.3 force source with quiet sun damping is roughly 1×10^{29} ergs; this is not unreasonable for such a strong flare, which may release up to 1×10^{32} ergs (Hudson 2011).

Moving forward, it is clear that sunquake signals are degenerate in parameter space with respect to source depth, and also time shift. The time shift degeneracy is relatively easy to deal with, as we expect the source to have timing close to the X-ray and bad pixel times, and this can be accounted for. The source depth degeneracy is more difficult to treat, as lower-amplitude deep sources can be compensated for by greater energy deposition. There are also several events - notably the X1.0 event - which indicate the presence of a high source, though such sources tend to produce weaker p-modes and stronger g-modes in the model as the height increases. Further study of atmospheric g-modes is necessary to understand their role in sunquake excitation and propagation.

In conclusion, we find that at least three sunquake events in the momentum source case and at least two events in the force source case are consistent with the electron beam hypothesis. The source start times of these events are coincident with or closely follow the time of peak HXR emission, which is a reliable diagnostic of energy deposition. In these cases, the energy required to excite the sunquakes falls within expectations based on previous studies, and in some cases indicates a moderate amount of acoustic damping in the region of sunquake propagation.

ACKNOWLEDGMENTS

The research was supported by NASA grants NNX14AB68G, NNX16AP05H, and NSF grant 1916509.

REFERENCES

- Antiochos, S. K., DeVore, C. R., & Klimchuk, J. A. 1999, *ApJ*, 510, 485
- Aptekar, R. L., Frederiks, D. D., Golenetskii, S. V., et al. 1995, *SSRv*, 71, 265
- Aschwanden, M. J. 2019, arXiv e-prints, arXiv:1909.08672
- Chen, R. 2019, PhD thesis, Stanford University
- Christensen-Dalsgaard, J. 2002, *Reviews of Modern Physics*, 74, 1073
- Christensen-Dalsgaard, J., Dappen, W., Ajukov, S. V., et al. 1996, *Science*, 272, 1286
- Courant, R., Friedrichs, K., & Lewy, H. 1967, *IBM J. Res. Dev.*, 11, 215. <http://dx.doi.org/10.1147/rd.112.0215>
- Couvidat, S., Schou, J., Hoeksema, J. T., et al. 2016, *SoPh*, 291, 1887
- E J Rhodes, J., Reiter, J., Schou, J., et al. 2011, *Journal of Physics: Conference Series*, 271, 012029. <https://doi.org/10.1088%2F1742-6596%2F271%2F1%2F012029>
- Fisher, G. H., Canfield, R. C., & McClymont, A. N. 1985, *ApJ*, 289, 414
- Hudson, H. S. 2011, *SSRv*, 158, 5
- Kopp, R. A., & Pneuman, G. W. 1976, *SoPh*, 50, 85
- Kosovichev, A. G. 2006, in *Astronomical Society of the Pacific Conference Series*, Vol. 354, *Solar MHD Theory and Observations: A High Spatial Resolution Perspective*, ed. J. Leibacher, R. F. Stein, & H. Uitenbroek, 154
- Kosovichev, A. G. 2015, *Sunquakes: Helioseismic response to solar flares*, in: *Extraterrestrial Seismology*, ed. V. Tong & R. Garcı, 306–322
- Kosovichev, A. G., & Zharkova, V. V. 1998, *Nature*, 393, 317
- Lysenko, A. L., Altyntsev, A. T., Meshalkina, N. S., Zhdanov, D., & Fleishman, G. D. 2018, ArXiv e-prints, arXiv:1802.09288
- Macrae, C., Zharkov, S., Zharkova, V., et al. 2018, *A&A*, 619, A65
- Pedram, E., & Matthews, S. A. 2012, *SoPh*, 277, 317
- Scherrer, P. H., Schou, J., Bush, R. I., et al. 2012, *SoPh*, 275, 207
- Sharykin, I., & Kosovichev, A. 2019, in *Solar Atmospheric and Interplanetary Environment (SHINE 2019 Conference)*, 204
- Sharykin, I. N., Kosovichev, A. G., Sadykov, V. M., Zimovets, I. V., & Myshyakov, I. I. 2017, *ApJ*, 843, 67

Singh, N. K., Raichur, H., & Brandenburg, A. 2016, ApJ,
832, 120

Ulyanov, A. S., Bogachev, S. A., Loboda, I. P., Reva, A. A.,
& Kirichenko, A. S. 2019, SoPh, 294, 128
Vranjes, J. 2014, Monthly Notices of the Royal
Astronomical Society, 445, 1614
Zharkova, V., & Zharkov, S. 2015, SoPh, 290, 3163